

SARS-CoV-2 spike glycoprotein vaccine candidate NVX-CoV2373 elicits immunogenicity in baboons and protection in mice

Jing-Hui Tian

Novavax (United States)

Nita Patel

Novavax (United States)

Robert Haupt

University of Maryland School of Medicine

Haixia Zhou

Novavax

Stuart Weston

University of Maryland, School of Medicine <https://orcid.org/0000-0001-9840-2953>

Holly Hammond

University of Maryland Baltimore

James Logue

University of Maryland School of Medicine <https://orcid.org/0000-0002-7410-9741>

Alyse Pornoff

Novavax, Inc.

James Norton

Novavax, Inc.

Mimi Guebre-Xabier

Novavax, Inc.

Bin Zhou

Novavax, Inc.

Kelsey Jacobson

Novavax, Inc.

Sonia Maciejewski

Novavax, Inc.

Rafia Khatoon

Novavax, Inc.

Malgorzata Wisniewska

Novavax, Inc.

Will Moffitt

Novavax, Inc.

Stefanie Kluefel-Stahl

Novavax, Inc.

Betty Ekechukwu

Novavax, Inc.

James Papin

University of Oklahoma Health Sciences Center <https://orcid.org/0000-0001-9894-8243>

Sarathi Boddapati

Catalent Paragon Gene Therapy

C. Jason Wong

Catalent Paragon Gene Therapy

Pedro Piedra

Baylor College of Medicine

Matthew Frieman

University of Maryland School of Medicine <https://orcid.org/0000-0003-0107-0775>

Michael Massare

Novavax (United States)

Louis Fries

Novavax, Inc.

Karin Lovgren Bengtsson

Novavax AB

Linda Stertman

Novavax AB

Larry Ellingsworth

Novavax, Inc

Gregory Glenn

Novavax (United States)

Gale Smith (✉ GSmith@Novavax.com)

Novavax (United States)

Article

Keywords: SARS-CoV-2, vaccine, NVX-CoV2373

Posted Date: July 15th, 2020

DOI: <https://doi.org/10.21203/rs.3.rs-39239/v1>

License:   This work is licensed under a Creative Commons Attribution 4.0 International License.

[Read Full License](#)

Version of Record: A version of this preprint was published at Nature Communications on January 14th, 2021. See the published version at <https://doi.org/10.1038/s41467-020-20653-8>.

Abstract

The COVID-19 pandemic continues to spread throughout the world with an urgent need for a safe and protective vaccine to effectuate herd immunity to control the spread of SARS-CoV-2. Here, we report the development of a SARS-CoV-2 subunit vaccine (NVX-CoV2373) produced from the full-length spike (S) protein, stabilized in the prefusion conformation. Purified NVX-CoV2373 S form 27.2 nm nanoparticles that are thermostable and bind with high affinity to the human angiotensin-converting enzyme 2 (hACE2) receptor. In mice and baboons, low-dose NVX-CoV2373 with saponin-based Matrix-M adjuvant elicits high titer anti-S IgG that is associated with blockade of hACE2 receptor binding, virus neutralization, and protection against SARS-CoV-2 challenge in mice with no evidence of vaccine-associated enhanced respiratory disease (VAERD). NVX-CoV2373 vaccine also elicits multifunctional CD4⁺ and CD8⁺ T cells, CD4⁺ T follicular helper T cells (Tfh), and the generation of antigen-specific germinal center (GC) B cells in the spleen. These results support the ongoing phase 1/2 clinical evaluation of the safety and immunogenicity of NVX-CoV2327 with Matrix-M (NCT04368988).

Introduction

Rapid global transmission of SARS-CoV-2 has followed the initial outbreak in Wuhan, Hubei Province, China first reported in December 2019. The World Health Organization's (WHO) 29 June 2020 COVID-19 Situation Report-160 reports 10 million confirmed cases worldwide and 500,000 deaths (5.1% fatality rate)¹⁻². Current estimates suggest a substantial asymptomatic incubation period during which transmission occurs, and a basic reproduction number (R0) of 2.23–2.51³, greater than any 20th or 21st century pandemic influenza virus. The urgent need for a safe, effective, stable, globally deployable, preventative vaccine has led to an unprecedented collaboration between vaccine developers, manufacturers, and distributors in concert with government and academic programs⁴.

The SARS-CoV-2 spike (S) glycoprotein is a major component of the virus envelope, essential for receptor binding, fusion, virus entry, and a target of host immune defense⁵⁻⁹. The SARS-CoV-2 S glycoprotein is a class I fusion protein produced as a large 1273 amino acid inactive precursor (S0). Unique to SARS-CoV-2 is the insertion of a polybasic RRAR furin-like cleavage motif in the S1/S2 cleavage site¹⁰. Proteolytic cleavage of the S-protein generates the S2 stalk that is conserved across human coronaviruses and the less conserved S1 cap¹¹. The N-terminal domain (NTD) and the receptor-binding domain (RBD) are located in the S1 subunit. The fusion peptide (FP), two heptad repeats (HR1 and HR2), central helix (CH), transmembrane (TM) domain, and cytoplasmic tail (CT) are located in the S2 subunit. Three S1/S2 protomers non-covalently associate to form the functional S-trimer. Like other fusion proteins, the SARS-CoV S-trimer is metastable and undergoes significant structural rearrangement from a prefusion conformation to a thermostable postfusion conformation upon S-protein receptor binding and proteolytic cleavage¹². Rearrangement exposes the hydrophobic FP allowing insertion into the host cell membrane, facilitating virus/host cell membrane alignment, fusion, and virus entry through endocytosis¹³⁻¹⁶.

We have developed a SARS-CoV-2 S subunit vaccine (NVX-CoV2373) constructed from the full-length S-protein and produced in the established Sf9 insect cell expression system. Here, we describe a stable prefusion S-protein structure generated by mutating the furin cleavage site to be resistant to cleavage and utilization of two proline substitutions at the apex of the central helix¹¹. Here, we show that administering the NVX-CoV2373 with Matrix-M adjuvant in a nonhuman primate and mice models induces a Th1 dominant B- and T-cell response, hACE2 receptor blocking antibodies and SARS-CoV-2 neutralizing antibodies. In mice, the vaccine was protective with no evidence of vaccine associated enhanced respiratory disease (VAERD). These results support the clinical development of the NVX-CoV2373 vaccine for prevention of COVID-19 (NCT04368988).

Results

SARS-CoV-2 spike glycoproteins. The SARS-CoV-2 S-gene (MN908947.3, nucleotides 21563–25384) encoding the full-length 1273 amino acid spike protein was used as a backbone to produce spike protein variants. The BV2365 single mutant was generated by mutating the putative furin cleavage site 682-RRAR-685 to 682-QQAQ-685, and the NVX-CoV2373 double mutant was generated with 682-QQAQ-685 and 2-proline substitutions at residues K986P and V987P (Fig. 1A). Synthetic full-length wild-type (WT), the single mutant BV2365, and double mutant NVX-CoV2373 genes were codon optimized for insect cells and cloned into recombinant baculovirus for expression in Sf9 cells.

Biophysical characterization and stability. Purified SARS-CoV-2 WT, BV2365, and NVX-CoV2373 S-proteins when reduced migrated with an apparent molecular weight of 180 kDa (Fig. 1B). Dynamic light scattering (DLS) showed the WT S-protein had a Z-average particle diameter of 69.53 nm compared to a 2-fold smaller particle size of BV2365 (33.4 nm) and NVX-CoV2373 (27.2 nm). The polydispersity index (PDI) indicated that BV2365 and NVX-CoV2373 particles were generally uniform in size, shape, and mass (PDI = 0.25–0.29) compared to the wild-type spike-protein (PDI = 0.46) (**Table 1 in the Supplementary Files**).

The thermal stability of the S-trimers was determined by differential scanning calorimetry (DSC). The thermal transition temperature of the WT S-spike ($T_{max} = 58.6\text{ }^{\circ}\text{C}$) was similar to BV2365 and NVX-CoV2373 with a $T_{max} = 61.3\text{ }^{\circ}\text{C}$ and $60.4\text{ }^{\circ}\text{C}$, respectively (**Table 1**). Of greater significance, was the 3–5 fold increased enthalpy of transition required to unfold the BV2365 and NVX-CoV2373 variants ($\Delta H_{cal} = 466$ and 732 kJ/mol , respectively) compared to the lower enthalpy required to unfold the WT spike protein ($\Delta H_{cal} = 153\text{ kJ/mol}$). These results are consistent with improved thermal stability of the BV2365 and NVX-CoV2373 compared to that of WT spike protein (**Table 1**).

Transmission electron microscopy (TEM) and 2D class averaging. TEM and two-dimensional (2D) class averaging were used to determine the ultrastructure of NVX-CoV2373. High magnification (67,000x and 100,000x) TEM images of negatively stained NVX-CoV2373 showed particles corresponding to S-protein homotrimers. An automated picking protocol supplemented with manual picking was used to construct 2D class average images^{17, 18}. Two rounds of 2D class averaging of homotrimeric structures revealed a

triangular particle appearance with a 15 nm length and 13 nm width (Fig. 1C, **top left**). Overlaying the recently solved cryoEM structure of the SARS-CoV-2 spike protein ectodomain (EMD ID: 21374)^{19,20} over the 2D NVX-Cov2373 image showed a good fit with the crown-shaped S1 (NTD and RBD) and the S2 stem (Fig. 1C, **bottom left**). Also apparent in the 2D images was a faint projection that protruded from the tip of the trimeric structure opposite of the NTD/RBD crown (Fig. 1C, **top right**). 2D class averaging using a larger box size showed these faint projections form a connection between the S-trimer and an amorphous structure. We speculate these faint projections likely represents the HR2 domain which is highly flexible in the prefusion conformation¹⁹ with the TM domain anchored within a polysorbate 80 micelle (Fig. 1C, **bottom right**).

SARS-CoV-2 S-protein binding to hACE2 receptor by BLI and ELISA. S-protein binding to the hACE2 receptor was determined using bio-layer interferometry (BLI). To assess binding, a histidine-tagged hACE2 receptor was coupled to nickel charged nitrilotriacetic acid (Ni-NTA) biosensor tips. The hACE2 coated biosensor tips were dipped in wells containing serially diluted (4.7 nM to 300 nM) recombinant S protein. Dissociation kinetics showed that the S-proteins remained tightly bound as evident by minimal or no dissociation over 900 seconds of observation in the absence of fluid-phase S protein (Fig. 2A, 2B, 2C).

We next determined the specificity of receptor binding using an ELISA method. In this evaluation, histidine-tagged hACE2 or hDPP-4 receptors over concentration range of 0.0001-5 $\mu\text{g mL}^{-1}$ were added to ELISA plates coated with WT, BV2365 or NVX-CoV2373 and binding was detected with HRP conjugated anti-histidine antibody. WT, BV2365, and NVX-CoV2373 proteins specifically bound hACE2 but failed to bind the hDPP-4 receptor used by MERS-CoV ($\text{IC}_{50} > 5000 \text{ ng mL}^{-1}$). WT and BV2365 bound to hACE2 with similar affinity ($\text{IC}_{50} = 36\text{--}38 \text{ ng mL}^{-1}$), while NVX-CoV2373 attained 50% saturation of hACE2 binding at 2-fold lower concentration ($\text{IC}_{50} = 18 \text{ ng mL}^{-1}$) (Fig. 2D, 2E, 2F).

SARS-CoV-2 S stability under stressed conditions. The stability of a COVID-19 vaccine for global distribution is critical. The structural integrity of the NVX-CoV2373 spike protein with the 2-prolines substitutions and BV2365 without the 2-proline substitutions was assessed with different environmental stress conditions using the hACE2 ELISA. Incubation of NVX-CoV2373 at pH extremes (48 hours at pH 4 and pH 9), with prolonged agitation (48 hours), through freeze/thaw (2 cycles), or elevated temperature (48 hours at 25 °C and 37 °C) had no effect on hACE2 receptor binding ($\text{IC}_{50} = 14.0\text{--}18.3 \text{ ng mL}^{-1}$). Only oxidizing conditions with hydrogen peroxide reduced the binding of NVX-CoV2373 by 8-fold ($\text{IC}_{50} = 120 \text{ ng mL}^{-1}$) (Fig. 3A). BV2365 without the 2-proline substitutions was less stable as determined by a significant reduction in hACE2 binding ($\text{IC}_{50} = 56.8\text{--}143.4 \text{ ng mL}^{-1}$) under multiple conditions (Fig. 3B). These results confirmed that the NVX-CoV2373 with the 2-proline mutation had significantly greater stability and was therefore selected for further evaluation.

NVX-CoV2373 vaccine immunogenicity in mice. We next assessed the immunogenicity of NVX-CoV2373 and the dose-sparing potential of saponin-based Matrix-M adjuvant. Groups of mice were immunized with a low dose range (0.01 μg , 0.1 μg , 1 μg and 10 μg) of NVX-CoV2373 with 5 μg Matrix-M adjuvant

using a single priming dose or a prime/boost regimen spaced 14-days apart. Animals immunized with a single priming dose of 0.1–10 µg NVX-CoV2373/Matrix-M had elevated anti-S IgG titers that were detected 21–28 days after a single immunization (Fig. 4A, **right**). Mice immunized with 10 µg dose of NVX-CoV2373/Matrix-M induced antibodies that blocked hACE2 receptor binding to S-protein and virus neutralizing antibodies 21–28-days after a single priming dose (Fig. 4B and 4C). Animals immunized with the prime/boost regimen had significantly elevated anti-S IgG titers that were detected 7–16 days following the booster immunization across all dose levels. Animals immunized with 1 µg and 10 µg NVX-CoV2373/Matrix-M had similar high anti-S IgG titers following immunization (GMT = 139,000 and 84,000, respectively). Importantly, mice immunized with 0.1 µg, 1 µg, or 10 µg NVX-CoV/Matrix-M had significantly ($p \leq 0.00001$) higher anti-S IgG titers compared to mice immunized with 10 µg NVX-CoV2373 without adjuvant (Fig. 4A, **left**). These results indicate the potential for a 10-fold or greater dose sparing provided by Matrix-M adjuvant. Furthermore, immunization with two doses of NVX-CoV2373/Matrix-M elicited high titer antibodies that blocked hACE2 receptor binding to S-protein ($IC_{50} = 218–1642$) and neutralized the cytopathic effect (CPE) of SARS-CoV-2 on Vero E6 cells (100% blocking of CPE = 7680–20,000) across all dose levels (Fig. 4B and 4C).

NVX-CoV2373 protection against SARS-CoV-2 in Ad/CMV/hACE2 mice. Mice were vaccinated with NVX-CoV2373 to evaluate the induction of protective immunity against challenge with SARS-CoV-2 by comparing single-dose or prime/boost vaccination strategies compared in a live virus challenge model. Mice were immunized with a single priming dose or a prime/boost regimen with NVX-CoV2373/Matrix-M as described above. Since mice do not support replication of wild-type SARS-CoV-2 virus, on day 52 post initial vaccination, mice were intranasally infected with an adenovirus expressing hACE2 (Ad/hACE2) to render them permissive. At four days post transduction, mice were challenged with 10^5 pfu/mouse of SARS-CoV-2 (WA1 strain). Following challenge mice were weighed daily and pulmonary histology and viral load were analyzed at day 4 and 7 post challenge.

At 4 days post infection, placebo-treated mice had an average of 10^4 SARS-CoV-2 pfu/lung, while the mice immunized with NVX-CoV2373 without Matrix-M had 10^3 pfu/lung and those with Matrix-M had limited to no detectable virus load (Fig. 4D). The NVX-CoV2373 with Matrix-M prime-only groups of mice exhibited a dose-dependent reduction in virus titer, with recipients of the 10 µg dose having no detectable virus at day 4 post infection. Mice receiving 1 µg, 0.1 µg and 0.01 µg doses all showed a marked reduction in titer compared to placebo-vaccinated mice. In the prime/boost groups, mice immunized with 10 µg, 1 µg and 0.1 µg doses had almost undetectable lung virus loads, while the 0.01 µg group displayed a reduction of at least 1 log relative to placebo animals. Weight loss during the experiment paralleled the viral load findings, with animals receiving single doses of 10 µg, 1 µg and 0.1 µg NVX-CoV2373/Matrix-M showing marked protection from weight loss compared to the unvaccinated placebo animals (Fig. 4E). The mice receiving a prime and boost vaccination with adjuvanted vaccine also demonstrated significant protection against weight loss at all dose levels (Fig. 4F). In addition, we compared the prime/boost regimens using 10 µg of either adjuvanted or unadjuvanted NVX-CoV2373. The mice receiving the prime/boost with adjuvant were significantly protected from weight loss relative to placebo mice, while

the group immunized with 10 µg NVX-CoV2373 alone were not protected against weight loss (Fig. 4G). These results confirm that NVX-CoV2373 confers protection against SARS-CoV-2 and that low doses of the vaccine associated with lower serologic responses do not exacerbate weight loss or demonstrate exaggerated illness.

Histopathology. Lung histopathology was evaluated on days 4 and day 7 post challenge. At day 4 post challenge, placebo-immunized mice showed denudation of epithelial cells in the large airways with thickening of the alveolar septa surrounded by a mixed inflammatory cell population. Periarteriol cuffing was observed throughout the lungs with inflammatory cells consisting primarily of neutrophils and macrophages. By day 7 post infection, the placebo-treated mice displayed peribronchiolar inflammation with increased periarteriol cuffing. The thickened alveolar septa remain with increased diffuse interstitial inflammation throughout the alveolar septa (Fig. 5).

The NVX-CoV2373 immunized mice showed significant reduction in lung pathology at both day 4 and day 7 post infection in a dose-dependent manner. The prime only group displays reduced inflammation at the 10 µg and 1 µg dose with a reduction in inflammation surrounding the bronchi and arterioles compared to placebo mice. In the lower doses of the prime-only groups, lung inflammation resembles that of the placebo groups, correlating with weight loss and lung virus titer. The prime/boost immunized groups displayed a significant reduction in lung inflammation for all doses tested, which again correlated with lung viral titer and weight loss data. The epithelial cells in the large and small bronchi at day 4 and 7 were substantially preserved with minimal bronchiolar sloughing or signs of viral infection. The arterioles of animals immunized with 10 µg, 1 µg and 0.1 µg doses have minimal inflammation with only moderate cuffing seen in the 0.01 µg dose, similar to placebo. Alveolar inflammation was reduced in animals that received the higher doses with only the lower 0.01 µg dose with inflammation (Fig. 5). These data demonstrate that NVX-CoV2373 reduces lung inflammation after challenge and that even doses and regimens of NVX-CoV2373 that elicit minimal or no detectable neutralizing activity are not associated with any obvious exacerbation of the inflammatory response to the virus.

Multifunctional cytokine analysis of CD4⁺ and CD8⁺ T cells in mice. To determine the role of Matrix-M in generating T cell responses, we immunized groups of mice (N = 6/group) with 10 µg NVX-CoV2373 alone or with 5 µg Matrix-M in a 2-dose regimen spaced 21-days apart. Antigen-specific T cell responses were measured by ELISPOT and intracellular cytokine staining (ICCS) from spleens collected 7-days after the second immunization (study day 28). The number of IFN-γ secreting cells after *ex vivo* stimulation increased 7-fold in spleens of mice immunized with NVX-CoV2373/Matrix-M compared to NVX-CoV2373 alone as measured by the ELISPOT assay (Fig. 6A). In order to examine CD4⁺ and CD8⁺ T cell responses separately, ICCS assays were performed in combination with surface marker staining. Data shown were gated on CD44^{hi} CD62L⁻ effector memory T cell population. Importantly, we found the frequency of IFN-γ⁺, TNF-α⁺, and IL-2⁺ cytokine-secreting CD4⁺ and CD8⁺ T cells was significantly higher (p < 0.0001) in spleens from the NVX-CoV2373/Matrix-M immunized mice compared to mice immunized without adjuvant (Fig. 6B and 6C). Further, we noted the frequency of multifunctional CD4⁺ and CD8⁺ T cells,

which simultaneously produce at least two or three cytokines was also significantly increased ($p < 0.0001$) in spleens from the NVX-CoV2373/Matrix-M immunized mice (Fig. 6B and 6C). Immunization with NVX-CoV2373/Matrix-M resulted in higher proportions of multifunctional phenotype within both CD4⁺ and CD8⁺ T cell populations. The proportions of multifunctional phenotypes detected in memory CD4⁺ T cells were higher than those in CD8⁺ T cells (Fig. 6D).

Type 2 cytokine IL-4 and IL-5 secretion from CD4⁺ T cells was also determined by ICCS and ELISPOT respectively. We found that immunization with NVX-CoV2373/Matrix-M also increased type 2 cytokine IL-4 and IL-5 secretion (2-fold) compared to immunization with NVX-CoV2373 alone, but to a lesser degree than enhancement of type 1 cytokine production (e.g. IFN- γ increased 20-fold). These results indicate that administration of the Matrix-M adjuvant led to an antigen-specific CD4⁺ T cell development, which was at least balanced between Th1 and phenotypes or, in most animals, Th1-dominant (**Supplementary Fig. 1**).

Having shown that vaccination with NVX-CoV2373/Matrix-M elicited multifunctional, antigen-specific, CD4⁺ T cell responses and virus neutralizing antibodies in mice, we next evaluated the effect of the immunization on germinal center formation by measuring the frequency of CD4⁺ T follicular helper (Tfh) and germinal center (GC) B cells in spleens. Addition of Matrix-M adjuvant significantly increased the frequency of Tfh cells (CD4⁺ CXCR5⁺ PD-1⁺) ($p = 0.01$), as well as the frequency of GC B cells (CD19⁺GL7⁺CD95⁺) ($p = 0.0002$) in spleens (Fig. 7A and 7B).

Immunogenicity NVX-CoV2373 vaccine in olive baboons. Having determined that low dose levels of NVX-CoV2373 with Matrix-M elicit protective neutralizing antibodies and promotes the generation of multifunctional antigen-specific T cells in mice, we next evaluated the immunogenicity of the vaccine in adult baboons. In this study, adult olive baboons were immunized with a dose range (1 μ g, 5 μ g and 25 μ g) of NVX-CoV2373 with 50 μ g Matrix-M adjuvant administered by IM injection in two doses spaced 21-days apart. To assess the adjuvant activity of Matrix-M in nonhuman primates, an additional group of animals was immunized with 25 μ g of NVX-CoV2373 without the adjuvant. Anti-S protein IgG titers were detected within 21-days of a single priming immunization in animals immunized with NVX-CoV2373/Matrix-M across all the dose levels (GMT = 1,249 – 19,000). Anti-S protein IgG titers increased over a log (GMT = 33,000-174,000) within 1 to 2 weeks following a booster immunization (days 28 and 35) across all of the dose levels. Importantly, animals immunized with NVX-CoV2373 without adjuvant had minimum or no detected anti-S IgG titer (GMT < 125) after one immunization, which was not boosted by a second immunization (Fig. 8A).

We also determined the functionality of the antibodies. Low levels of hACE2 receptor blocking antibodies were detected in animals following a single immunization with 5 or 25 μ g NVX-CoV2373/Matrix-M (GMT = 22–37). Receptor blocking antibody titers were significantly increased within one to two weeks of the booster immunization across all groups immunized with NVX-CoV2373/Matrix-M (GMT = 150–600) (Fig. 8B). Virus neutralizing antibodies were also elevated (GMT = 190–446) across all dose groups after a single immunization with NVX-CoV2373/Matrix-M. Animals immunized with 25 μ g NVX-CoV2373 alone had no detectable antibodies that block S-protein binding to hACE2 (Fig. 8B). Neutralizing titers increased

25- to 38-fold following the second immunization (GMT = 6,400 – 17,000) (Fig. 8C). Animals receiving the NVX-CoV2373 alone had little or no detectable neutralizing antibodies (GMT < 100). There was a significant correlation ($p < 0.0001$) between anti-S IgG levels and neutralizing antibody titers (Fig. 8D). The immunogenicity of the adjuvanted vaccine in nonhuman primates is consistent with the mouse immunogenicity results and further supports the role of Matrix-M adjuvant in promoting the generation of neutralizing antibodies and dose sparing.

PBMCs were collected 7 days after the second immunization (day 28) and T cell response was measured by ELISPOT assay. PBMCs from animals immunized with 5 μ g or 25 μ g NVX-CoV2373/Matrix-M had the highest number of IFN- γ secreting cells, which was 5-fold greater on average compared to animals immunized with 25 μ g NVX-CoV2373 alone or 1 μ g NVXCoV2373/Matrix-M (Fig. 8E). By ICCS analysis, immunization with 5 μ g NVXCoV2373/Matrix-M also showed the highest frequency of IFN- γ^+ , IL-2 $^+$, and TNF- α^+ CD4 $^+$ T cells (Fig. 8F). This trend was also true for multifunctional CD4 $^+$ T cells, in which at least two or three type 1 cytokines were produced simultaneously (Fig. 8F). Type 2 cytokine IL-4 level were too low to be detected in baboons by ELISPOT analysis.

We next compared the levels of serum antibodies in recovered COVID-19 patients to the level of antibodies in NVX-CoV2373/Matrix-M vaccinated baboons. The mean anti-S IgG levels were 7-fold higher in immunized baboons (EC50 = 152,060, 95%CI, 60,767 – 243,354) compared to convalescent serum (EC50 = 21,136, 95%CI, 11,473 – 30,799). We also compared the level of functional hACE2 receptor inhibiting (50% RI) titers. Baboons receiving the vaccine had 8-fold higher binding and receptor inhibiting antibodies (50% RI = 478, 95%CI, 161.1-794.4) compared to COVID-19 convalescent serum (50% RI = 61, 95%CI, 35.7–85.5) (Fig. 9). Therefore, NVX-CoV2373 vaccine induced binding and functional antibodies in a nonhuman primate at levels comparable or higher than individuals recovered from COVID-19. Collectively these results support the development of NVX-CoV2373 for prevention of COVID-19

Discussion

Here, we showed that a full-length, stabilized prefusion SARS-CoV-2 spike glycoprotein vaccine (NVX-CoV2373) adjuvanted by Matrix-M can induce high levels of functional immunity in mice and baboons, and protects mice expressing hACE2 receptors in a live SARS-CoV-2 challenge. The functional immunity induced by the nanoparticle vaccine and Matrix-M adjuvant is clearly dependent on both the adjuvant and antigen components and mirrors the human experience with influenza hemagglutinin vaccine²¹ and a naïve population with ebola recombinant protein nanoparticle vaccines²². Immunization with NVX-CoV2373 at low doses in mice and nonhuman primate induced anti-S antibodies, hACE2-receptor inhibiting antibodies, and SARS-CoV-2 neutralizing antibodies after one dose with significantly increased titers after a booster immunization. In addition, NVX-CoV2373 vaccine induced CD4 $^+$ and CD8 $^+$ T cell responses, and in mice provided protection against SARS-CoV-2 challenge. Matrix-M adjuvant was also shown to enhance Tfh cell and GC B cell development, which are critical for induction and maintaining of

high affinity antibody response. Low, suboptimal doses of NVX-CoV2373 vaccine did not show evidence of VAERD in challenged mice^{23, 24}.

While multiple animal models have been developed for infection with human coronaviruses, including SARS, MERS, and now COVID19, to date none of them fully represent the pathology or clinical symptoms of human infection. However, the murine hACE2 transduced challenge model with wild-type virus appears to recapitulate the severe clinical disease seen in humans, although the pathological basis for illness may differ. Of note, the adenovirus-based hACE-2 transduction itself gives rise to some background inflammatory changes which are present in all animals and are, of course, not responsive to prophylaxis targeting SARS-CoV-2. This may make histopathology in this model less responsive to the vaccine than parameters such as weight loss. Nonetheless, by blocking and ameliorating the common initiating event, hACE-2 receptor binding, vaccine-induced functional immunity is demonstrated that indicates a potential for the vaccine to induce a protective immunity. Models utilizing macaques and baboons specifically have been predictive for human immunogenicity and suggest this vaccine should continue to be evaluated in these systems as well as in humans. To this end, the safety, immunogenicity, and efficacy of the NVX-CoV2373 with Matrix-M adjuvant is currently being evaluated in multiple nonhuman primate models and a phase 1/2 clinical trial (NCT04368988).

Methods

Cell lines, virus, antibody reagents, and receptors. Vero E6 cells (ATCC, CRL-1586) were maintained in Minimal Eagles Medium (MEM) supplemented with 10% fetal bovine serum, 1% glutamine and 1% penicillin and streptomycin. The SARS-CoV-2 (WA-1) isolated was obtained from the Center for Disease Control (WA-1 strain) and stock virus prepared in Vero E6 cells. Histidine-tagged hACE2 and histidine-DPP4 receptors were purchased from Syno Biologics (Beijing, CN). Rabbit anti-SARS-CoV spike protein was purchased from Biodefense and Emerging Infections Research Resources Repository (catalog no. NR-4569, BEI Resources, Manassas, VA).

SARS-CoV-2 protein expression. SARS-CoV-2 constructs were synthetically produced from the full-length S glycoprotein gene sequence (GenBank MN908947 nucleotides 21563–25384). The full-length S-genes were codon optimized for expression in *Spodoptera frugiperda* (Sf9) cells and synthetically produced by GenScript (Piscataway, NJ, USA). The QuikChange Lightning site-directed mutagenesis kit (Agilent) was used to produce two spike protein variants: modifications by mutating the S1/S2 cleavage site by mutation of the furin cleavage site (682-RRAR-685) to 682-QQAQ-685 to be protease resistant and designated as BV2365. The single mutant BV2365 was further stabilized by introducing two proline substitutions at positions K986P and V987P (2P) to produce the double mutant, NVX-CoV2373. Full-length S-genes were cloned between the BamHI – HindIII sites in the pFastBac baculovirus transfer vector (Invitrogen, Carlsbad, CA) under transcriptional control of the *Autographa californica* polyhedron promoter. Recombinant baculovirus constructs were plaque purified and master seed stocks prepared and used to produce the working virus stocks. The baculovirus master and working stock titers were determined using

rapid titer kit (Clontech, Mountain View, CA). Recombinant baculovirus stocks were prepared by infecting Sf9 cells with a multiplicity of infection (MOI) of ≤ 0.01 plaque forming units (pfu) per cell²⁵⁻²⁷.

Expression and purification. SARS-CoV-2 S proteins were produced in Sf9 cells expanded in serum-free medium to a density of $2-3 \times 10^6$ cell mL⁻¹ and infected with recombinant baculovirus at MOI of ≤ 0.1 pfu per cell. Cells were cultured at 27 ± 2 °C and harvested at 68–72 hours post-infection by centrifugation (4000 x g for 15 min). Cell pellets were suspended in 25 mM Tris HCl (pH 8.0), 50 mM NaCl and 0.5-1.0% (v/v) TERGITOL NP-9 with leupeptin. S-proteins were extracted from the plasma membranes with Tris buffer containing NP-9 detergent, clarified by centrifugation at 10,000 x g for 30 min. S-proteins were purified by TMAE anion exchange and lentil lectin affinity chromatography. Hollow fiber tangential flow filtration was used to formulate the purified spike protein at 100–150 $\mu\text{g mL}^{-1}$ in 25 mM sodium phosphate (pH 7.2), 300 mM NaCl, 0.02% (v/v) polysorbate 80 (PS 80)²⁶. Purified S-proteins were evaluated by 4–12% gradient SDS-PAGE stained with Gel-Code Blue reagent (Pierce, Rockford, IL) and purity was determined by scanning densitometry using the OneDscan system (BD Biosciences, Rockville, MD).

Dynamic light scattering (DLS). Samples were equilibrated at 25 °C and scattering intensity was monitored as a function of time in a Zetasizer NanoZS (Malvern, UK). Cumulants analysis of the scattered intensity autocorrelation function was performed with instrument software to provide the z-average particle diameter and polydispersity index (PDI).

Differential scanning calorimetry (DCS). Samples and corresponding buffers were heated from 4 °C to 120 °C at 1 °C per minute and the differential heat capacity change was measured in a NanoDSC (TA Instruments, New Castle, DE). A separate buffer scan was performed to obtain a baseline, which was subtracted from the sample scan to produce a baseline-corrected profile. The temperature where the peak apex is located is the transition temperature (T_{max}) and the area under the peak provides the enthalpy of transition (ΔH_{cal}).

Transmission electron microscopy (TEM) and 2D class averaging. Electron microscopy was performed by Nanolmaging Services (San Diego, CA) with a FEI Tecani T12 electron microscope, operated at 120 keV equipped with a FEI Eagle 4 k x 4 k CCD camera. SARS-CoV-2 S proteins were diluted to $2.5 \mu\text{g mL}^{-1}$ in formulation buffer. The samples (3 μL) were applied to nitrocellulose-supported 400-mesh copper grids and stained with uranyl formate. Images of each grid were acquired at multiple scales to assess the overall distribution of the sample. High-magnification images were acquired at nominal magnifications of $110,000 \times$ (0.10 nm/pixel) and $67,000 \times$ (0.16 nm/pixel). The images were acquired at a nominal under focus of $-1.4 \mu\text{m}$ to $-0.8 \mu\text{m}$ (110,000x) and electron doses of $\sim 25 \text{ e}/\text{\AA}^2$.

For class averaging, particles were identified at high magnification prior to alignment and classification. The individual particles were selected, boxed out, and individual sub-images were combined into a stack to be processed using reference-free classification. Individual particles in the 67,000x high magnification images were selected using an automated picking protocol¹⁷. An initial round of alignments was

performed for each sample, and from the alignment class averages that appeared to contain recognizable particles were selected for additional rounds of alignment. These averages were used to estimate the percentage of particles that resembled single trimers and oligomers. A reference-free alignment strategy based on XMIPP processing package was used for particle alignment and classification¹⁸.

Kinetics of SARS-CoV-2 S binding to hACE2 receptor by BLI. S-protein receptor binding kinetics was determined by bio-layer interferometry (BLI) using an Octet QK384 system (Pall Forté Bio, Fremont, CA). Hist-tagged human ACE2 ($2 \mu\text{g mL}^{-1}$) was immobilized on nickel-charged Ni-NTA biosensor tips. After baseline, SARS-CoV-2 S protein containing samples were 2-fold serially diluted over a range 4.7 nM to 300 nM range were allowed to associate for 600 sec followed by dissociation for an additional 900 sec. Data was analyzed with Octet software HT 101:1 global curve fit.

Specificity of SARS-CoV-2 S binding to hACE2 receptor by ELISA. Ninety-six well plates were coated with 100 μL SARS-CoV-2 spike protein ($2 \mu\text{g mL}^{-1}$) overnight at 4 °C. Plates were washed with phosphate buffered saline with 0.05% Tween (PBS-T) buffer and blocked with TBS Startblock blocking buffer (ThermoFisher, Scientific). Histidine-tagged hACE2 and hDPP4 receptors were 3-fold serially diluted ($5-0.0001 \mu\text{g mL}^{-1}$) and added to coated wells for 2 hours at room temperature. The plates were washed with PBS-T. Optimally diluted horseradish peroxidase (HRP) conjugated anti-histidine was added and color developed by addition of and 3,3',5,5'-tetramethylbenzidine peroxidase substrate (TMB, T0440-IL, Sigma, St. Louis, MO, USA). Plates were read at an OD of 450 nm with a SpectraMax Plus plate reader (Molecular Devices, Sunnyvale, CA, USA) and data analyzed with SoftMax software. EC_{50} values were calculated by 4-parameter fitting using GraphPad Prism 7.05 software

Animal ethics statement. The mouse immunogenicity studies were performed by Noble Life Sciences (Sykeville, MD). Noble Life Sciences is accredited by the Association for Assessment and Accreditation of Laboratory Animal Care (AAALACC International). All animal procedures were in accordance with NRC Guide for the Care and Use of Laboratory Animals, the Animal Welfare Act, and the CDC/NIH Biosafety in Microbiological and Biomedical Laboratories. The olive baboon (*Papio cynocephalus anubis*) study was performed at the University of Oklahoma Health Science Center (OUHSC). OUHSC is accredited by AAALACC International. Baboons were maintained and treated according to the Institutional Biosafety Committee guidelines. Baboon experiments were approved by the Institutional Animal Care and Use Committee (IACUC) and the Institutional Biosafety Committee of OUHSC. Studies were conducted in accordance with the National Institutes of Health Guide for Care and Use of Laboratory Animals (NIH publication 8023, Revised 1978).

Mouse study designs. Female BALB/c mice (7–9 weeks old, 17–22 grams, N = 10 per group) were immunized by intramuscular (IM) injection with a single dose (study day 14) or two doses spaced 14-days apart (study day 0 and 14) containing a dose range (0.01, 0.1, 1.0, or 10 μg) of NVX-CoV2373 with 5 μg saponin-based Matrix-M™ adjuvant (Novavax, AB, Uppsala, SE). A separate group (n = 10) received two doses of 10 μg NVX-CoV2373 without adjuvant. A placebo group served as a non-immunized control.

Serum was collected for analysis on study days - 1, 13, 21, and 28. Vaccinated and control animals were intranasally challenged with SARS-CoV-2 42-days following one or two immunizations (study day 56).

To assess the T cell response mediated by Matrix-M adjuvant, groups of female BALB/c mice (N = 6 per group) were immunized IM with 10 µg NVX-CoV2373 with and without 5 µg Matrix-M adjuvant in 2 doses spaced 21-days apart. Spleens were collected 7-days after the second immunization (study day 28). A non-vaccinated group (N = 3) served as a control.

Baboon study design. Ten adult baboons (10–16 years of age) were randomized into 4 groups of 2–3/group and immunized by IM injection with 1, 5 or 25 µg NVX-CoV2373 with 50 µg Matrix-M adjuvant. A separate group was immunized with 25 µg NVX-CoV2373 without adjuvant. Animals were vaccinated with 2-doses spaced 21-days apart. Serum was collected on study days 0, 21, 28 and 35. For T cell analysis, peripheral blood mononuclear cells (PBMCs) were collected 7-days after the second immunization (study day 28). Subsequent to the start of the study one animal tested positive for STLV and was therefore dropped from the study.

SARS-CoV-2 challenge in mice. Mice were transduced intranasally with 2.5×10^8 pfu Ad/CMVhACE2 (VVC-McCray-7580, University of Iowa Vector Core) 38-days after the second vaccination. At four days post infection, mice were anaesthetized by intraperitoneal injection 50 µL of a mix of xylazine (0.38 mg/mouse) and ketamine (1.3 mg/mouse) diluted in phosphate buffered saline (PBS). Mice were intranasally inoculated with 1.5×10^5 pfu of SARS-CoV-2 in 50 µL divided between nares. Challenged mice were weighed on day of infection and daily for up to 7 days post infection. At days 4- and 7-days post infection, 5 mice were sacrificed from each vaccination and control group, and lungs were harvested to determine for titer by a plaque assay and prepared for histological scoring.

SARS-CoV-2 plaque assay. SARS-CoV-2 lung titers were quantified by homogenizing harvested lungs in PBS (Quality Biological Inc.) using 1.0 mm glass beads (Sigma Aldrich) and a Beadruptor (Omini International Inc.). Homogenates were added to Vero E6 near confluent cultures and SARS-CoV-2 virus titers determined by counting plaque forming units (pfu) using a 6-point dilution curve.

Anti-SARS-CoV-2 spike IgG by ELISA. An ELISA was used to determine anti-SARS-CoV-2 S IgG titers. Briefly, 96 well microtiter plates (ThermoFischer Scientific, Rochester, NY, USA) were coated with $1.0 \mu\text{g mL}^{-1}$ of SARS-CoV-2 spike protein. Plates were washed with PBS-T and blocked with TBS Startblock blocking buffer (ThermoFisher, Scientific). Mouse, baboon or human serum samples were serially diluted (10^{-2} to 10^{-8}) and added to the blocked plates before incubation at room temperature for 2 hours. Following incubation, plates were washed with PBS-T and HRP-conjugated goat anti-mouse IgG or goat anti-human IgG (Southern Biotech, Birmingham, AL, USA) added for 1 hour. Plates were washed with PBS-T and 3,3',5,5'-tetramethylbenzidine peroxidase substrate (TMB, T0440-IL, Sigma, St Louis, MO, USA) was added. Reactions were stopped with TMB stop solution (ScyTek Laboratories, Inc. Logan, UT). Plates were read at OD 450 nm with a SpectraMax Plus plate reader (Molecular Devices, Sunnyvale, CA, USA) and data analyzed with SoftMax software. EC_{50} values were calculated by 4-parameter fitting using

SoftMax Pro 6.5.1 GxP software. Individual animal anti-SARS-CoV-2 S IgG titers and group geometric mean titers (GMT) and 95% confidence interval (\pm 95% CI) were plotted GraphPad Prism 7.05 software.

ACE2 receptor blocking antibodies. ACE2 receptor blocking antibodies were determined by ELISA. Ninety-six well plates were coated with $1.0 \mu\text{g mL}^{-1}$ SARS-CoV-2 S protein overnight at 4°C . Serially diluted serum from groups of immunized mice, baboons or humans were added to coated wells and incubated for 2 hours at room temperature. After washing, 30 ng mL^{-1} of histidine-tagged hACE or hDPP4 was added to wells for 1 hour at room temperature. HRP-conjugated anti-histidine IgG was added followed by washing prior to addition of TMB substrate. Plates were read at OD 450 nm with a SpectraMax plus plate reader (Molecular Devices, Sunnyvale, CA, USA) and data analyzed with SoftMax software. Serum dilution resulting in a 50% inhibition of receptor binding was used to calculate titer determined using 4-parameter fitting with GraphPad Prism 7.05 software.

SARS-CoV-2 neutralization assay. SARS-CoV-2 was handled in a select agent ABSL3 facility at the University of Maryland, School of Medicine. Mouse or baboon sera were diluted 1:20 in Vero E6 cell growth media and further diluted 1:2 to 1:40960. SARS-CoV-2 (MOI of 0.01 pfu per cell) was added and the mixture incubated for 60 min at 37°C . Vero E6 media was used as negative control. The inhibitory capacity of each serum dilution was assessed for cytopathic effect (CPE). The endpoint titer was reported as the dilution that blocked 100% of CPE at 3 days post infection.

ELISPOT assay. Murine IFN- γ and IL-5 ELISPOT assays were performed following manufacturer's procedures for mouse IFN- γ and IL-5 ELISPOT kit (Mabtech, Cincinnati, OH). Briefly, 3×10^5 splenocytes in a volume of 200 μL were stimulated with NVX-CoV2373 protein or peptide pools (PP) of 15-mer peptides with 11 overlapping amino acids covering the entire spike protein sequence (JPT, Berlin, Germany) in plates that were pre-coated with anti-IFN- γ or anti-IL-5 antibodies. Each stimulation condition was carried out in triplicate. Assay plates were incubated overnight at 37°C in a 5% CO_2 incubator and developed using BD ELISPOT AEC substrate set (BD Biosciences, San Diego, CA). Spots were counted and analyzed using an ELISPOT reader and Immunospot software (Cellular Technology, Ltd., Shaker Heights, OH). The number of IFN- γ or IL-5 secreting cells was obtained by subtracting the background number in the medium controls. Data shown in the graph are the average of triplicate wells.

Similarly, Baboon IFN- γ and IL-4 assays were carried out using NHP IFN- γ and Human IL-4 assay kit from Mabtech using PBMC collected at day 7 following the second immunization (day 28).

Surface and intracellular cytokine staining. For surface staining, murine splenocytes were first incubated with an anti-CD16/32 antibody to block the Fc receptor. To characterize T follicular helper cells (Tfh), splenocytes were incubated with the following antibodies or dye: BV650-conjugated anti-CD3, APC-H7-conjugated anti-CD4, FITC-conjugated anti-CD8, Percp-cy5.5-conjugated anti-CXCR5, APC-conjugated anti-PD-1, Alexa Fluor 700-conjugated anti-CD19, PE-conjugated anti-CD49b (BD Biosciences, San Jose, CA) and the yellow LIVE/DEAD[®] dye (Life Technologies, NY). To stain germinal center (GC) B cells, splenocytes were labeled with FITC-conjugated anti-CD3, PerCP-Cy5.5-conjugated anti-B220, APC-

conjugated anti-CD19, PE-cy7-conjugated anti-CD95, and BV421-conjugated anti-GL7 (BD Biosciences) and the yellow LIVE/DEAD® dye (Life Technologies, NY).

For intracellular cytokine staining (ICCS) of murine splenocytes, cells were cultured in a 96-well U-bottom plate at 2×10^6 cells per well. The cells were stimulated with NVX-CoV2373 or pools of a 15-mer peptide pool (PP) as described above (JPT, Berlin, Germany). The plate was incubated 6 h at 37 °C in the presence of BD GolgiPlug™ and BD GolgiStop™ (BD Biosciences). Cells were labeled with murine antibodies against CD3 (BV650), CD4 (APC-H7), CD8 (FITC), CD44 (Alexa Fluor 700), and CD62L (PE) (BD Pharmingen, CA) and the yellow LIVE/DEAD® dye. After fixation with Cytotfix/Cytoperm (BD Biosciences), cells were incubated with PerCP-Cy5.5-conjugated anti-IFN- γ , BV421-conjugated anti-IL-2, PE-cy7-conjugated anti-TNF- α , and APC-conjugated anti-IL-4 (BD Biosciences). All stained samples were acquired using a LSR-Fortessa flow cytometer (Becton Dickinson, San Jose, CA) and the data were analyzed with FlowJo software version Xv10 (Tree Star Inc., Ashland, OR).

For ICCS, baboon PBMCs were collected 7 days after the second immunization (day 28) and stimulated as described above with NVX-CoV2373. Cells were labelled with human/NHP antibodies BV650-conjugated anti-CD3, APC-H7-conjugated anti-CD4, APC-conjugated anti-CD8, BV421-conjugated anti-IL-2, PerCP-Cy5.5-conjugated anti-IFN- γ , PE-cy7-conjugated anti-TNF- α (BD Biosciences), and the yellow LIVE/DEAD® dye.

Histopathology. Mice were euthanized at 4- and 7-days following SARS-CoV-2 challenge. The lungs were fixed with 10% formalin, and sections were stained with H&E for histological examination. Slides were examined in a blinded fashion for total inflammation, periarteriolar, and peribronchiolar inflammation and epithelial cell denuding.

COVID-19 convalescent serum. Convalescent serum samples were provided by Dr. Pedro A Piedra (Baylor College of Medicine, Houston, TX, USA). Samples were collected from COVID-19 patients 18–79 years of age 4–6 weeks after testing positive for SARS CoV-2. Symptoms ranged from asymptomatic, mild to moderate symptoms, to severe symptoms requiring hospitalization. Sera were analyzed for anti-SARS-CoV-2 S IgG and hACE2 receptor inhibiting antibody levels.

Statistical analysis. Statistical analyses were performed with GraphPad Prism 7.05 software (La Jolla, CA). Serum antibody titers were plotted for individual animals and the geometric mean titer (GMT) and 95% confidence interval (95% CI) or the means \pm SEM as indicated in the figure. T-test was used to determine differences between paired groups. Weight change between immunized and placebo groups was determined for each day using a t-test. P-values \leq 0.05 were considered as statistically significant.

Declarations

Data availability

The authors declare that all data supporting the findings of the study are available in the article and the Supplementary Information file. No computer codes are required.

Competing interests

Authors JHT, NP, HZ, ADP, JN, MGX, BZ, KJ, SM, RK, MW, WM, SKS, SE, MJM, SB, CJW, LF, KLB, LS, GG, LE and GS are current or past employees of Novavax, Inc., a for-profit organization, and these authors own stock or hold stock options. These interests do not alter the authors' adherence to policies on sharing data and materials. MBF, RH, SW, JL, HH, PAP and JP declare no competing interests.

Author contributions

GS, GG, JHT, NP, RH, HZ, MGX, ADP, MJM, MBF and LE contributed to conceptualization of experiments, generation of data and analysis, and interpretation of the results. JHT, RH, NP, SW, HH, JL, JN, BZ, KJ, SM, RK, MW, WM, SKS, BE, SB, CJW, HZ performed experiments. ADP, MGX, JP coordinated projects. MBF, ADP, MJM, LF, PAP, KLB, LS, GG, GS, LE contributed to drafting and making critical revisions with the help of others.

Acknowledgments

Funding for certain studies was provided by the Coalition for Epidemic Preparedness Innovations, PO Box 123, Torshov, 0412 Oslo, Norway.

References

1. Xu J et al. Systematic Comparison of Two Animal-to-Human Transmitted Human Coronaviruses: SARS-CoV-2 and SARS-CoV. *Viruses*. **12**, 244 (2020). doi: 10.3390/v1202024.
2. Lai CC, Shih TP, Ko WC, Tang HJ, Hsueh PR. Severe acute respiratory syndrome coronavirus 2 (SARS-CoV-2) and coronavirus disease-2019 (COVID-19): The epidemic and the challenges. *Int J Antimicrob Agents*. **17**, 105924 (2020). doi: 10.1016/j.ijantimicag.2020.105924.
3. Huang R, Liu M, Ding Y. Spatial-temporal distribution of COVID-19 in China and its prediction: A data-driven modeling analysis. *J Infect Dev Ctries*. **14**, 246–253 (2020). doi: 10.3855/jidc.12585.
4. Corey L, Mascola JR, Fauci AS, Collins FS. A strategic approach to COVID-19 vaccine R&D. *Science*. **368**, 948–950 (2020). doi: 10.1126/science.abc5312.
5. Walls AC et al. Tectonic conformational changes of a coronavirus spike glycoprotein promote membrane fusion. *Proc Natl Acad Sci U S A*. **114**, 11157–11162 (2017). doi: 10.1073/pnas.1708727114.
6. Ding Y et al. The clinical pathology of severe acute respiratory syndrome (SARS): a report from China. <http://www.J Pathol>. **200**, 282–289 (2003). doi: 10.1002/path.1440.
7. Tang XC et al. Identification of human neutralizing antibodies against MERS-CoV and their role in virus adaptive evolution. *Proc Natl Acad Sci U S A*. **111**, E2018-2026 (2014). doi:

- 10.1073/pnas.1402074111.
8. Li F. et al. Structure, Function, and Evolution of Coronavirus Spike Proteins. *Annu Rev Virol.* **3**, 237–261 (2016). doi: 10.1146/annurev-virology-110615-042301.
 9. Bosch BJ, van der Zee R, de Haan CA, Rottier PJ. The coronavirus spike protein is a class I virus fusion protein: structural and functional characterization of the fusion core complex. *J Virol.* **77**, 8801–8811 (2003). doi: 10.1128/jvi.77.16.8801-8811.2003.
 10. Coutard B, Valle C, de Lamballerie X, Canard B, Seidah NG, Decroly E. The spike glycoprotein of the new coronavirus 2019-nCoV contains a furin-like cleavage site absent in CoV of the same clade. *Antiviral Res.* **176**, 04742 (2020). doi: 10.1016/j.antiviral.2020.104742.
 11. Pallesen J et al. Immunogenicity and structures of a rationally designed prefusion MERS-CoV spike antigen. *Proc Natl Acad Sci U S A.* 2017, 114, E7348-E7357. doi: 10.1073/pnas.1707304114.
 12. Walls AC, Park YJ, Tortorici MA, Wall A, McGuire AT, Veesler D. Structure, Function, and Antigenicity of the SARS-CoV-2 Spike Glycoprotein. *Cell.* **181**, 281–292 (2020). <https://doi.org/10.1016/j.cell.2020.02.058>
 13. Raj VS et al. Dipeptidyl peptidase 4 is a functional receptor for the emerging human coronavirus-EMC. *Nature.* **495**, 251–254 (2013). doi: 10.1038/nature12005.
 14. Millet JK, Whittaker GR. Host cell entry of Middle East respiratory syndrome coronavirus after two-step, furin-mediated activation of the spike protein *Proc Natl Acad Sci U S A.* **111**, 15214–9 (2014). doi: 10.1073/pnas.1407087111.
 15. Belouzard S, Chu VC, Whittaker GR. Activation of the SARS coronavirus spike protein via sequential proteolytic cleavage at two distinct sites. *Proc Natl Acad Sci U S A.* **106**, 5871–5876 (2009). doi: 10.1073/pnas.0809524106.
 16. Li W et al. Angiotensin-converting enzyme 2 is a functional receptor for the SARS coronavirus. *Nature.* **426**, 450–454 (2003). doi: 10.1038/nature02145.
 17. Lander GC et al. Appion: an integrated, database-driven pipeline to facilitate EM image processing. *J Struct Biol.* **166**, 95–102 (2009).
 18. Sorzano CO et al. XMIPP: a new generation of an open-source image processing package for electron microscopy. *J Struct Biol.* **148**, 194–204 (2004).
 19. Wrapp D, et al. Cryo-EM structure of the 2019-nCoV spike in the prefusion conformation. *Science.* **367**, 1260–1263 (2020). doi: 10.1126/science.abb2507.
 20. Ou X et al. Characterization of spike glycoprotein of SARS-CoV-2 on virus entry and its immune cross-reactivity with SARS-CoV. *Nat Commun.* **11**, 1620 (2020). doi: 10.1038/s41467-020-15562-9.
 21. Shinde V et al. Improved Titers against Influenza Drift Variants with a Nanoparticle Vaccine. *N Engl J Med.* **378**, 2346–2348 (2018). doi: 10.1056/NEJMc1803554.
 22. 10.1093/infdis/jiz518
Fries L et al. A Randomized, Blinded, Dose-Ranging Trial of an Ebola Virus Glycoprotein (EBOV GP) Nanoparticle Vaccine with Matrix-M™ Adjuvant in Healthy Adults. *J Infect Dis.* jiz518 (2019).

<https://doi.org/10.1093/infdis/jiz518>.

23. Liu L et al. Anti-spike IgG causes severe acute lung injury by skewing macrophage responses during acute SARS-CoV infection. *JCI Insight*. **4**, e123158 (2019). doi: 10.1172/jci.insight.123158.
24. Gralinski LE et al. Complement Activation Contributes to Severe Acute Respiratory Syndrome Coronavirus Pathogenesis. *mBio*. **9**, e01753 (2018). doi: 10.1128/mBio.01753-18.
25. Liu YV et al. Chimeric severe acute respiratory syndrome coronavirus (SARS-CoV) S glycoprotein and influenza matrix 1 efficiently form virus-like particles (VLPs) that protect mice against challenge with SARS-CoV. *Vaccine*. **29**, 6606–6613 (2011). doi: 10.1016/j.vaccine.2011.06.111.
26. Coleman CM et al. Purified coronavirus spike protein nanoparticles induce coronavirus neutralizing antibodies in mice. *Vaccine*. **32**, 3169–3174 (2014). doi: 10.1016/j.vaccine.2014.04.016.
27. Coleman CM et al. MERS-CoV spike nanoparticles protect mice from MERS-CoV infection. *Vaccine*. **35**, 1586–1589 (2017). doi: 10.1016/j.vaccine.2017.02.012.

Figures

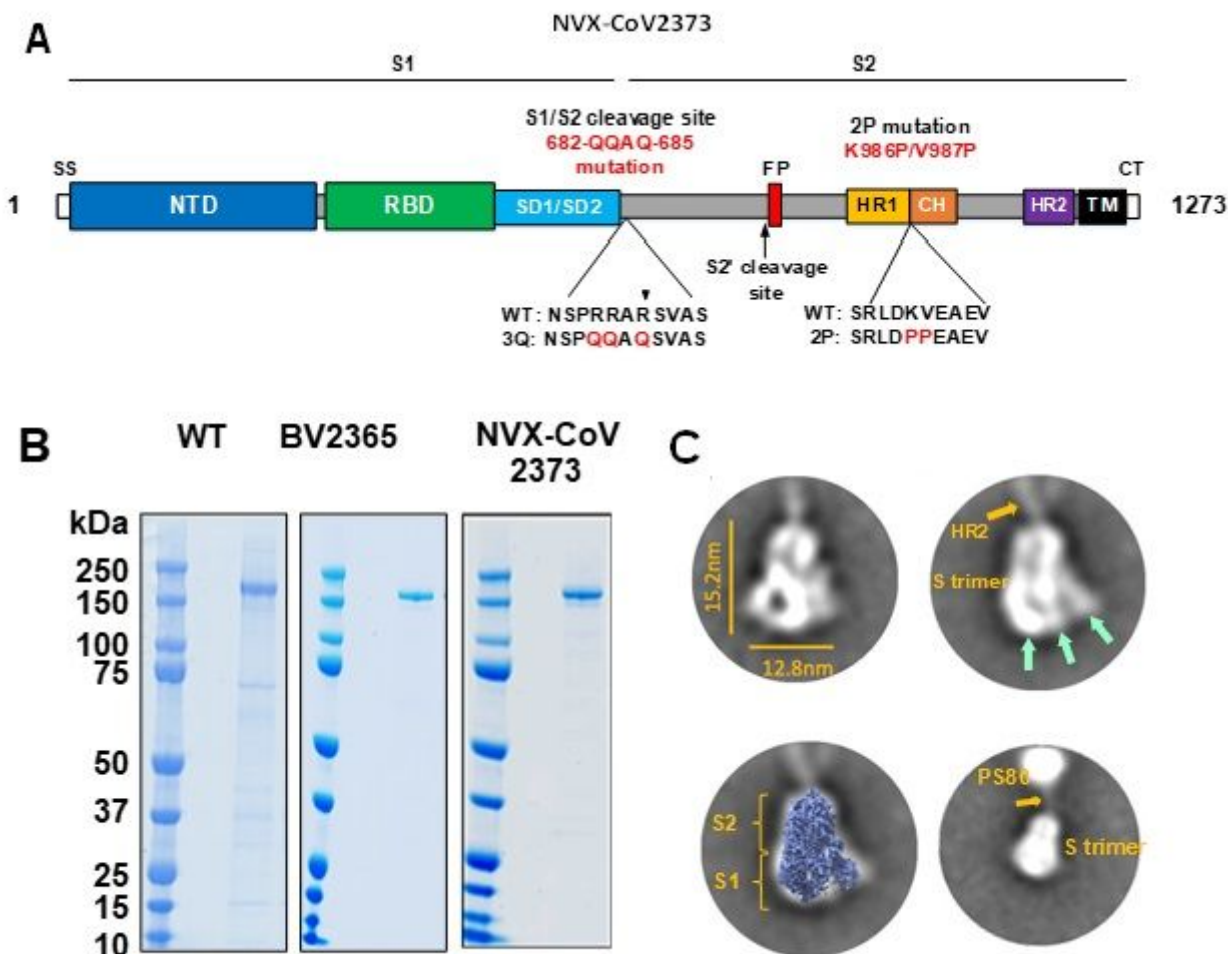


Figure 1

SARS-CoV-2 spike glycoprotein constructs. (A) Linear diagram of the full-length SARS-CoV-2 spike (S) protein showing the S1 and S2 subunits. Structural elements include a cleavable signal sequence (SS, white), N-terminal domain (NTD, blue), receptor binding domain (RBD, green), subdomains 1 and 2 (SD1/SD2, light blue), fusion peptide (FP, red), heptad repeat 1 (HR1, yellow), central helix (CH, brown), heptad repeat 2 (HR2, purple), transmembrane domain (TM, black) and cytoplasmic tail (CT, white). The native furin cleavage site was mutated (RRAR→QQAQ) to be protease resistant to generate the full-length BV2365 variant. The BV2365 was further stabilized by introducing two proline (2P) substitutions at positions K986P and V987P to produce the double mutant NVX-CoV2373. (B) Representative reduced SDS-PAGE gel of purified full-length wild-type (WT), BV2365, and NVX-CoV2373. (C) Transmission electron microscopy and 2D class averaging of NVX-CoV2373. Representative class averages of NVX-CoV2373 S-trimers showing well-defined triangle shaped particles with a length of 15 nm and a width of 12.8 nm (upper left). The S1 apical surface with the N-terminal receptor and receptor-binding domain (NTD/RBD) is indicated by green arrows. Faint protrusions (orange arrow) extending from the tip of the trimers were evident and appear to correspond to the S2 HR2 domain (upper right). Class average images showing a good fit of NVX-CoV2373 S-trimer with cryoEM solved structure of the SARS-CoV-2 trimeric spike protein ectodomain (EMD ID: 21374) overlaid on the 2D image (lower left). 2D class averaging using a larger box sized showing 2D class average image with the less well-defined HR2 (orange arrow) anchoring the S-trimer to polysorbate 80 (PS80) micelle by the C-terminal TM (lower right).

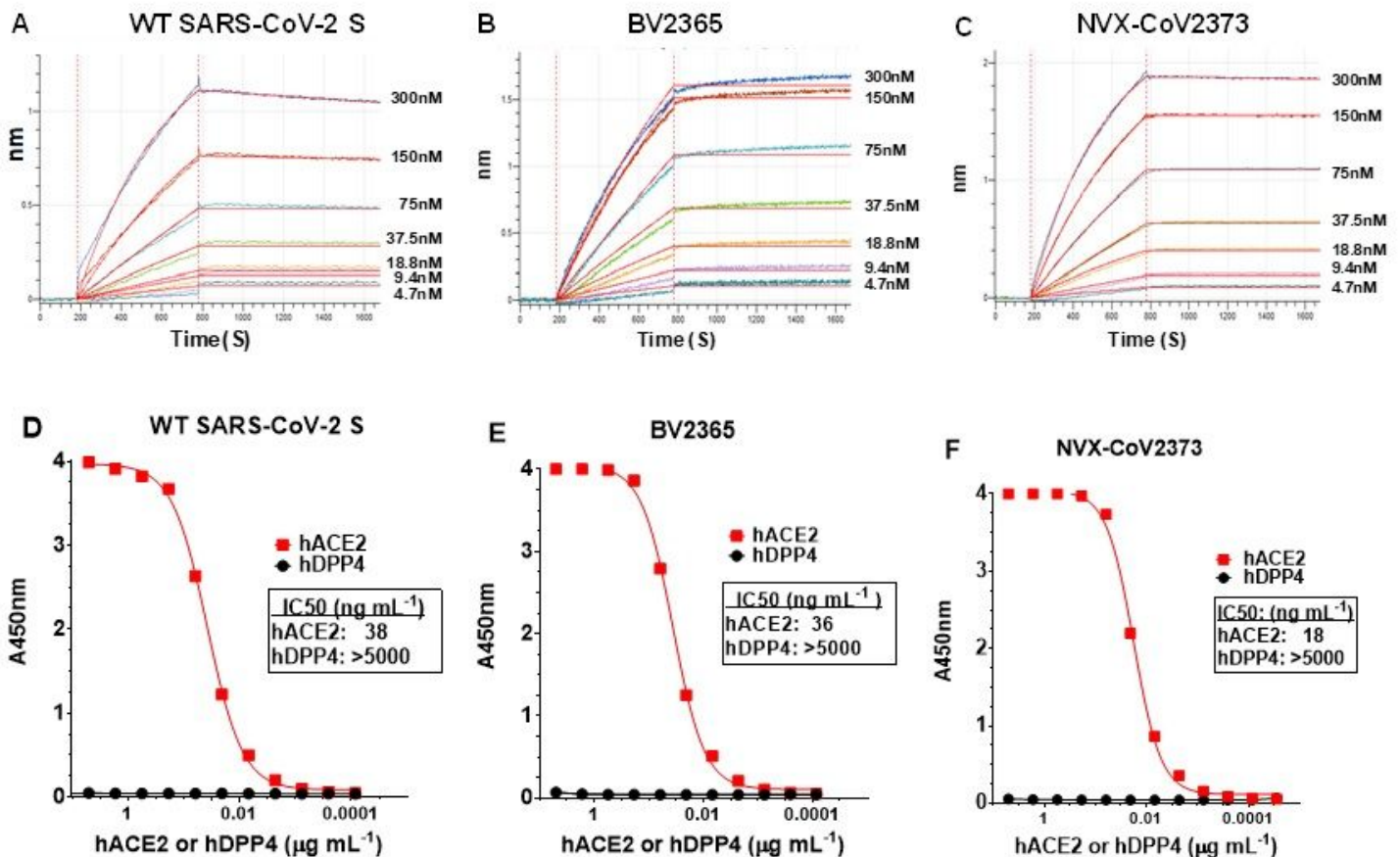


Figure 2

Kinetics and specificity of SARS-CoV-2 S protein binding to hACE2 receptor determined by bio-layer interferometry (BLI) and ELISA. BLI sensorgram showing the binding of (A) wild-type (WT), (B) BV2365, and (C) NVX-CoV2373 spike proteins to histidine-tagged hACE2 receptor immobilized on a Ni-NTA biosensor tip. Data are shown as colored lines at different concentrations of spike protein. Red lines are the best fit of the data. (D) WT-SARS-CoV-2 S, (E) BV2365, and (F) NVX-CoV2373 demonstrated by binding to hACE2 receptor but failing to bind hDPP-4 as determined by ELISA.

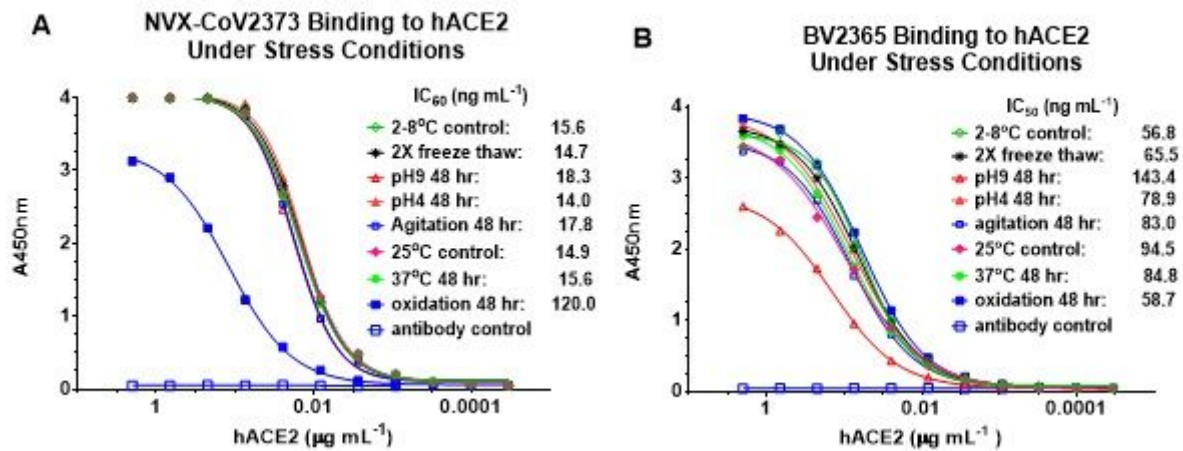


Figure 3

Stability of SARS-CoV-2 variants under stress conditions. The hACE2 receptor binding ELISA method was used to assess the structural integrity of BV2365 and NVXCoV2373 under stressed conditions. (A) NVXCoV2373 and (B) BV2365 were exposed to repeat freeze-thaw cycles, pH extremes, agitation, elevated temperatures, and oxidation for extended periods as indicated. Treated samples were immobilized on 96-well plates then incubated with serially diluted (2- 0.0001 µg mL⁻¹) histidine-tagged hACE2. Bound receptor was detected with HRP-conjugated rabbit anti-histidine IgG.

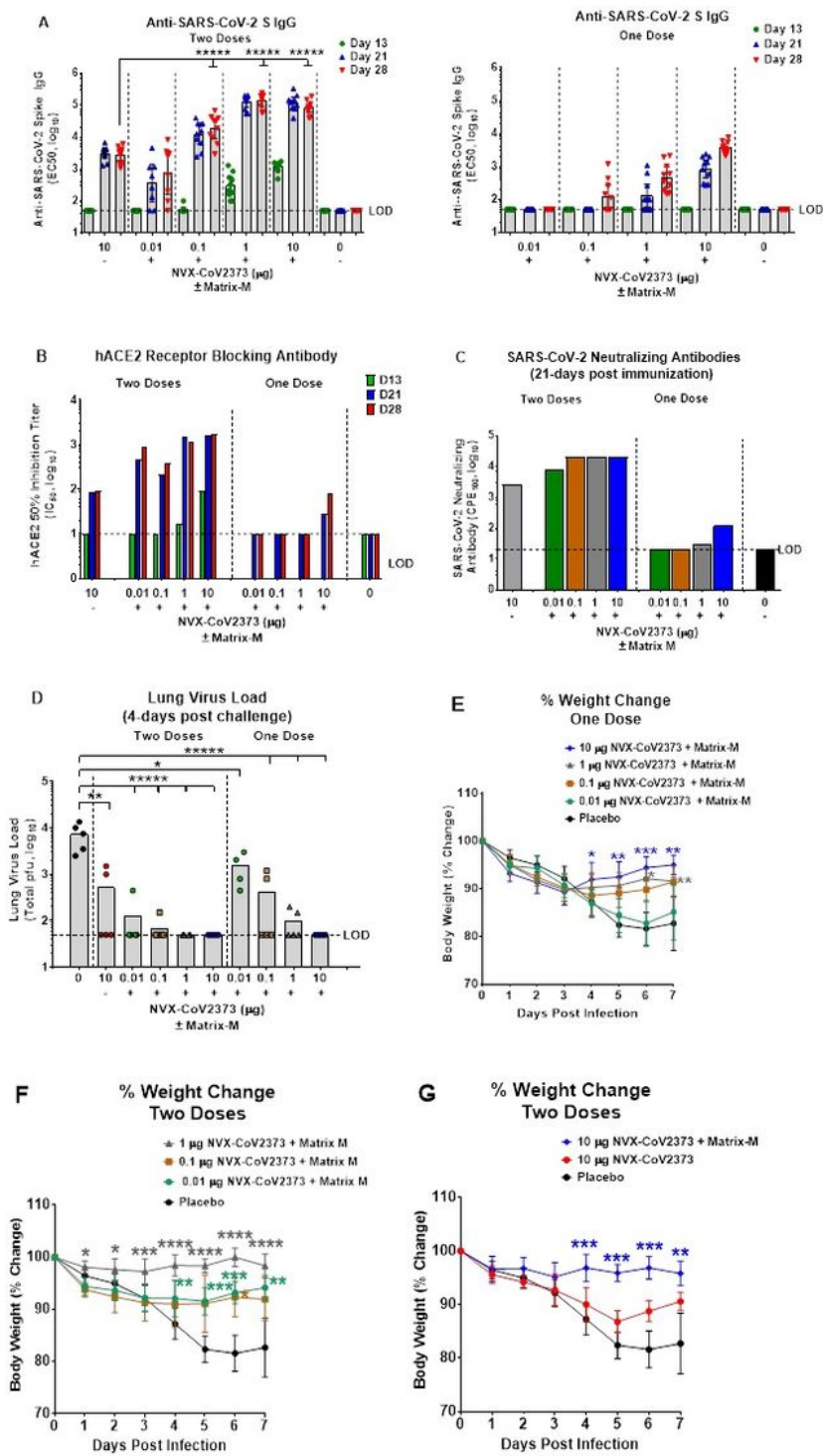


Figure 4

Immunogenicity of NVX-CoV2373 vaccine and protection against SARS-CoV-2 infection in mice. Groups of mice (N =10 per group) were immunized with a single priming dose (study day 14) or a prime/boost spaced 14 days apart (study day 0 and 14) over a low dose range (0.01-10 µg) NVX-CoV2373 with Matrix-M adjuvant (5 µg). (A) Anti-SARS-CoV-2 S IgG results are plotted as the geometric mean titer (GMT and 95% CI). (B) Human ACE2 receptor blocking antibodies in pooled serum (N = 10/group). (C) SARS-CoV-2

virus neutralizing antibody titers in pooled serum (N = 10/group). Six weeks following the booster immunization (study day 52) mice were transduced intranasally with 2.5×10^8 pfu Ad/CMVhACE2. At 4-days post infection mice were intranasally challenged with 1.5×10^5 pfu of SARS-CoV-2. Animals were monitored daily for up to 7-days post infection. (D) Infectious virus load in lung homogenates at 4-days post SARS-CoV-2 challenge. Bars represent the mean titers (N = 5 per group). (E, F, G) Weight change following nasal challenge with SARS-CoV-2. Results are plotted as the mean \pm SD (N = 5-10/time point). Data plotted as the mean \pm SD. T-test was used to compare differences in weight change of vaccinated groups to the non-vaccinated placebo control group. * $p \leq 0.05$, ** $p \leq 0.001$, *** $p \leq 0.0001$, **** $p \leq 0.000001$. Limit of detection (LOD).

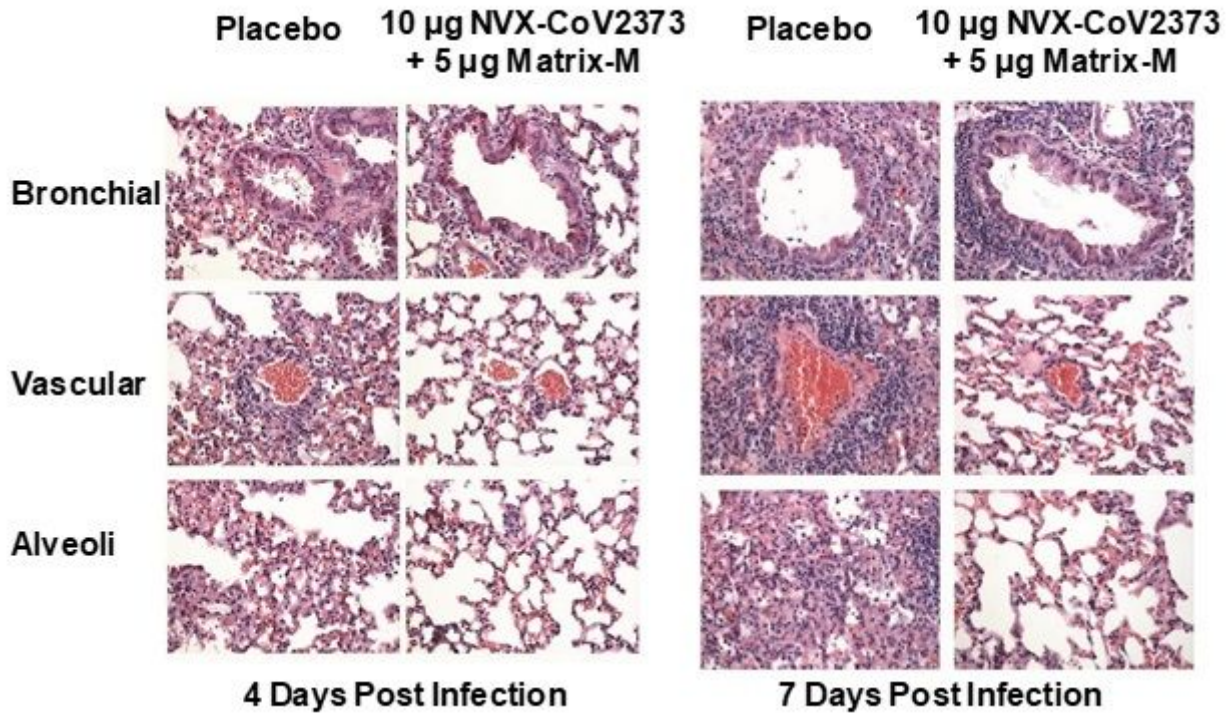


Figure 5

Representative histopathology of lungs from NVX-CoV2373 vaccinated and Ad/CMV/hACE2 transduced mice challenged with SARS-CoV-2. Groups of mice were vaccinated with NVX-CoV2373 with Matrix-M adjuvant with 2-doses spaced 14 days apart. Mice were intranasally infected with Ad/CMV/hACE2 31-days following the first immunization. On study day 56, mice were challenged with 1×10^5 pfu/mouse of SARS-CoV-2 (WA1 strain). Lungs were collected 4- and 7-days post infection. Representative placebo control animal at 4-days post infection showing denuding of bronchial epithelium with marked thickening of the alveolar septa surrounded by a mixed inflammatory cells. Diffuse periarteriolar cuffing throughout the lung consisting of a neutrophils and macrophages. At 7-days post infection, peribronchiolar inflammation and periarteriolar cuffing was markedly increased. Lungs from NVX-CoV2373 vaccinated animals had little or no epithelial cell sloughing or infection within large and small bronchi at day 4 and 7 post infection. There was no evidence of exacerbated lung inflammation in NVX-CoV2373 immunized animals.

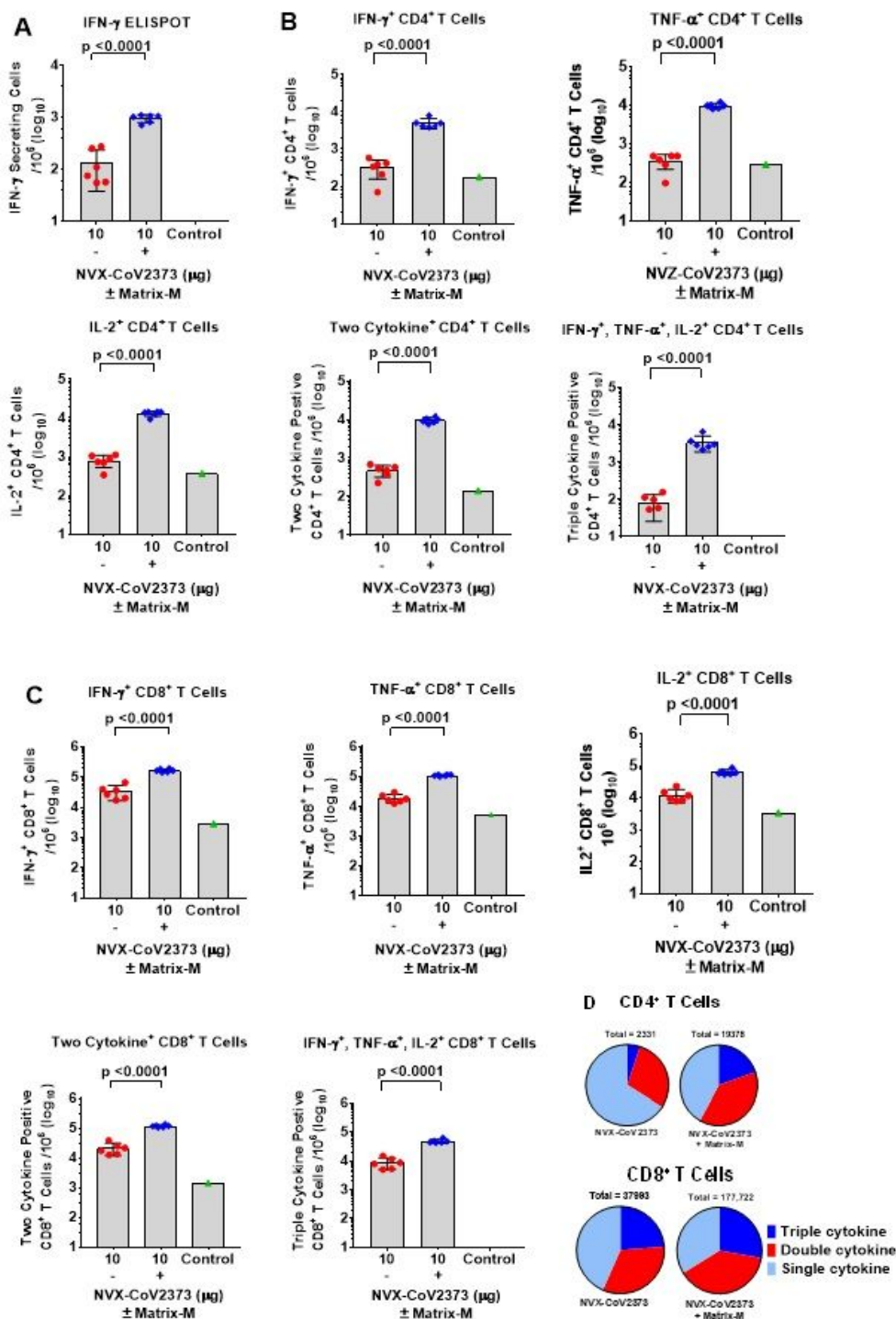


Figure 6

Multifunctional cytokine analysis of SARS-CoV-2 S-specific CD4⁺ and CD8⁺ T cells in immunized mice. Groups of mice (N = 6/group) were immunized with 10 μ g NVX-CoV2373 with and without 5 μ g Matrix-M adjuvant in 2 doses spaced 21-days apart. A negative control group (N = 3) was not immunized. Splenocytes were collected 7-days after the second immunization (day 28) and stimulated with a peptide pool (PP) that covers the entire spike protein for 6 hours. (A) The number of IFN- γ secreting cells per

million splenocytes was determined by ELISPOT. (B and C) The frequency of CD4+ memory T cells and CD8+ memory T cells producing IFN- γ , TNF- α , and IL-2, or at least 2 of 3 cytokines was determined by intracellular cytokine staining (ICCS). Analyzed cells were gated on the CD44hiCD62L- effector memory population. Bars represent the mean values and the error bars indicate \pm SEM. Significant differences between groups vaccinated with and without adjuvant are indicated. (D) Pie charts represent the relative proportion of CD4+ and CD8+ T cells producing one, two, or three cytokines (IFN- γ , TNF- α , and IL-2) in mice immunized with NVX-CoV2373 antigen with and without adjuvant.

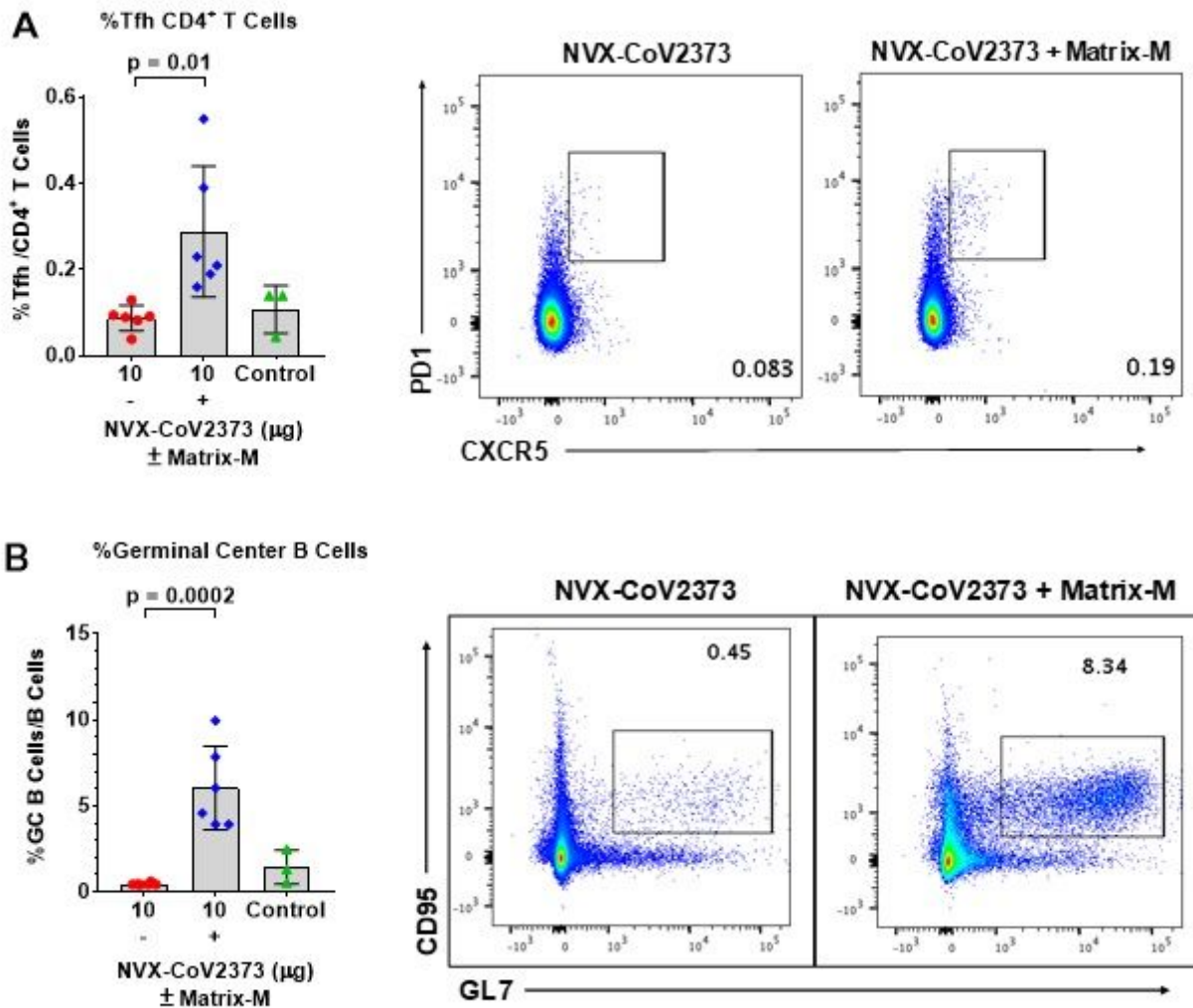


Figure 7

Frequencies of follicular helper T cell (Tfh) and germinal center (GC) B cells generated by immunization with NVX-CoV2373 and Matrix-M adjuvant. Mice were immunized with NVX-CoV2373 with and without Matrix-M adjuvant and splenocytes were collected 7-days after the second immunization. (A) The frequency of splenic Tfh cells (CXCR5+ PD-1+ CD4+) in the CD4 T population. (B) The frequency of splenic germinal center (GC) B cells (GL7+ CD95+ CD19+) in B cells. Bars represent the mean values and the error bars indicate \pm SEM. Significant differences between groups are indicated.

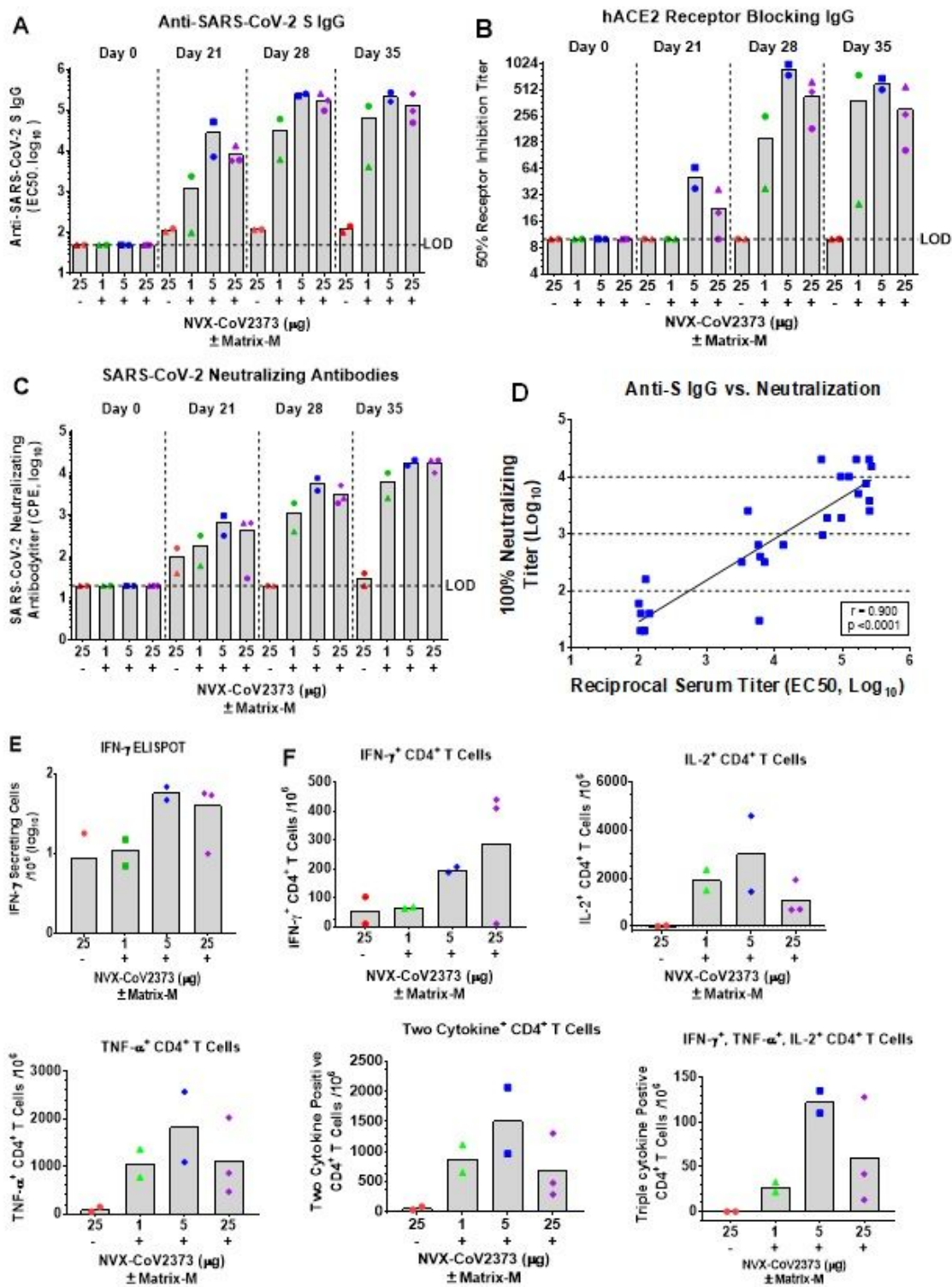


Figure 8

Humoral and cellular immune response to NVX-CoV2373 with and without Matrix-M adjuvant in baboons. Baboons were randomly assigned to groups (N = 2-3/group) and immunized by IM injection with 1, 5, or 25 μ g of NVX-CoV2373 and 50 μ g Matrix-M adjuvant in 2-doses spaced 21-days apart (D0 and D21). A separate group (N = 2) received 2-doses of 25 μ g NVX-CoV2373 without adjuvant. For serologic analysis, serum was collected prior to immunization (D0) and 21, 28, 35 and 49 days after the first immunization.

(A) Anti-SARS-CoV-2 S IgG titers were determined by ELISA. (B) human ACE2 receptor blocking antibodies were determined by ELISA. (C) SARS-CoV-2 neutralizing antibodies determined by in vitro inhibition of cytopathic effect (CPE). Bars represent mean titers. Limit of detection (LOD). (D) Correlation of anti-SARS-CoV-2 S IgG titers vs SARS CoV-2 neutralizing antibodies. Peripheral blood mononuclear cells (PBMCs) were collected 7-days after the second immunization (study day 28) and re-stimulated with NVX-CoV2373 spike protein. (E) IFN- γ -secreting PBMCs re-stimulated with NVX-CoV2373 protein were determined by ELISPOT. (F) Frequency of SARS-CoV-2 spike-specific CD4+ T cells producing single and multiple combinations of type 1 cytokines IFN- γ , TNF- α , and IL-2 determined by intracellular cytokine staining (ICCS). Solid bars represent the mean values.

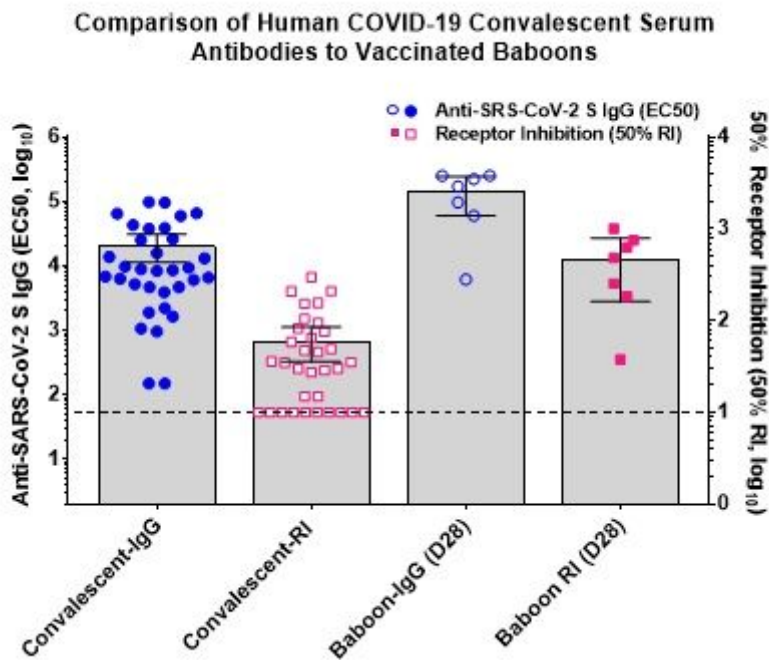


Figure 9

Comparison of COVID-19 human convalescent serum antibody levels to NVX-CoV2373 vaccinated baboon antibody levels. Convalescent serum was collected from recovered COVID-19 patients 4-6 weeks after testing positive for SARS-CoV-2. Sera were analyzed for anti-SARS-CoV-2 S IgG and human ACE2 receptor inhibition antibody levels (50% RI) and antibody levels compared to levels in serum of NVX-CoV2373 with Matrix-M immunized baboons as described in Fig. 8. The bars represent the group mean and error bars indicate the 95% confidence interval. Dashed line indicates the limit of detection (LOD).

Supplementary Files

This is a list of supplementary files associated with this preprint. Click to download.

- [NVXCoV2373SupplementaryInformation.docx](#)
- [Table1.pdf](#)